Acta Astronautica 219 (2024) 48–59

Contents lists available at ScienceDirect

Acta Astronautica

journal homepage: www.elsevier.com/locate/actaastro

Research paper

Towards an optimized heat transfer process in vaporizing liquid microthrusters using pulsed heating control

D. Fontanarosa [a], D. Van Langenhove [a], M.A. Signore [b], M.G. De Giorgi [c,*], L. Francioso [b], J. Steelant [d], M.R. Vetrano [a]

[a] KU Leuven, Department of Mechanical Engineering, Division of Applied Mechanics and Energy Conversion (TME), B-3001 Leuven, Belgium
[b] Italian National Research Council - Institute for Micro-electronics and Micro-systems (CNR-IMM), Via per Monteroni "Campus Ecotekne", Lecce, Italy
[c] Department of Engineering for Innovation, University of Salento, via per Monteroni, Lecce I-73100, Italy
[d] Flight Vehicles and Aerothermodynamics Engineering Section, ESTEC-ESA, Keplerlaan 1, 2200AG Noordwijk, The Netherlands

ARTICLE INFO

Keywords:
Electric micro-propulsion
Small satellites
Vaporizing liquid microresistojet
MEMS technology
Pulsed heating

ABSTRACT

The Institute for Microelectronics and Microsystems of the Italian National Research Council (Italy) has designed and fabricated a water-fed MEMS vaporizing liquid microthruster (VLM) in collaboration with the University of Salento (Italy) and KU Leuven (Belgium). Previous studies have demonstrated the device's functioning and highlighted the presence of a strong thermoelectric-hydraulic coupling that severely affects the heating and propulsive efficiencies and reliability of the device. In this regard, the current work provides a preliminary experimental investigation of a pulsed heating system actively controlled by temperature using PI-D logic (proportional and integrative actions applied to the error; derivative action applied to the output). The overall performance assessment focuses on evaluating power consumption during steady-state operation and analyzing the dynamic response of the VLM undergoing such an actively controlled pulsed heating, which has been built using both manual and data-driven offline adaptive tuning of the PID parameters. Concerning the steady-state operation, results highlight a promising enhancement of the heating efficiency to values above 0.9. The dynamic response analysis shows that operating with a single set of fixed PID parameters is not feasible and that the manual tuning is a trial-and-error approach highly dependent on the operator's experience, operating conditions, and reference temperature profile. Furthermore, shorter rise and response times require a higher proportional gain, and the overshoot experienced when crossing the saturation temperature cannot be avoided. In this paper, we show that the response of the data-driven adaptive controller solves these issues, exhibiting a reduced maximum settling time from around 59 s to less than 10 s, while the overshoot is avoided thanks to the temporal adjustment of the PID parameters.

1. Introduction

Secondary micro-propulsion systems easily integrated onboard small satellites for fine attitude control and position pointing have become a promising solution driven by the recent development of micro-electro-mechanical systems (MEMS) technology. In this regard, the simplicity of the concept and the use of lighter and smaller propellant tanks make vaporizing liquid microthrusters (VLMs) an interesting choice. VLMs can provide thrust force ranging between 0.1 and 10 mN with a nominal specific impulse between 50 s and 100 s using water as a green propellant [1]. The first water-fueled MEMS-based VLM studies date back to the end of the '90s with Mueller's works [2–4], followed by continuous and independent research activities involving different configurations, materials, and manufacturing technologies [5]. For instance, concerning the silicon technology, Mukejee et al. [6] first used wet anisotropic etching, while Maurya et al. [7] designed and fabricated a silicon-based VLM with an integrated micro-heater and, later, Kundu et al. [8] developed a new device design using two heaters integrated on the silicon substrate to ensure uniform heating. Instead, Ye et al. [9] applied an electric pulse producing an impulse bit of about 2 μN s. More recently, Silva et al. [10] developed a VLM with embedded molybdenum heaters, which was integrated into the

* Correspondence to: Department of Engineering for Innovation, Research Center for Energy and Environment (UNISALENTO-DII-CREA), University of Salento, via per Monteroni, Lecce I-73100, Italy.
E-mail addresses: donato.fontanarosa@kuleuven.be (D. Fontanarosa), dries.vanlangenhove@kuleuven.be (D. Van Langenhove), mariaassunta.signore@cnr.it (M.A. Signore), mariagrazia.degiorgi@unisalento.it (M.G. De Giorgi), lucanunzio.francioso@cnr.it (L. Francioso), johan.steelant@esa.it (J. Steelant), rosaria.vetrano@kuleuven.be (M.R. Vetrano).

https://doi.org/10.1016/j.actaastro.2024.02.041
Received 23 January 2024; Received in revised form 18 February 2024; Accepted 26 February 2024
Available online 28 February 2024

Nomenclature

Symbols

DC	Duty cycle, [–]
f_{pulse}	Pulse frequency, [Hz]
I	Electrical current, [A]
K_P	Proportional gain, [–]
$\dot{m}$	Mass flow rate, [ml/h] or [kg/s]
N_w	Number of selected distances, [count]
$\%OS$	Percent overshoot, [%]
$oHTP$	Overall heat transfer process, [J/kgK]
P_d	Measured power consumption, [W]
P_{ideal}	Ideal power consumption, [W]
P_{loss}	Power consumption losses, [W]
$\dot{Q}_H$	Heat required for full vaporization and overheat, [W]
$\dot{Q}_R$	Joule heating of the main resistive heater, [W]
t	Time variable, [s]
T_D	Derivative time, [s]
T_I	Integrative time, [s]
T_{set}	Setpoint temperature, [°C]
T_{TC1}	Thermocouple reading at the inlet chamber, [°C]
T_{TC2}	Thermocouple reading at the microchannel entrance, [°C]
V	Applied voltage, [V]

Greek Symbols

$\eta_{heating}$	Heating efficiency, [–]
$\phi(t)$	Information vector at time t
σ_{Pd}	Unbiased standard deviation of the power consumption, [W]
τ_{rise}	Response rise time, [s]
τ_{set}	Response settling time, [s]
$\theta^{PID}(t)$	Control vector at time t

Abbreviations

CNR-IMM	Italian National Research Council - Institute for Micro-electronics and Micro-systems
DD	Data-Driven
MEMS	Micro-Electro-Mechanical System
MOSFET	Metal–Oxide–Semiconductor Field Effect Transistor
PID	Proportional–Integrative–Derivative
PVC	PolyVinylChloride
PWM	Pulse Width Modulation
RTD	Resistance Temperature Detector
VLM	Vaporizing Liquid Microthruster

attitude control system of CubeSats and PocketQubes. In contrast, Liu et al. [11,12] developed and tested two VLM concepts using induction heating, characterized by tubular and planar geometry. Furthermore, for thrust forces below 300 μN, novel concepts of capillary-fed MEMS microthrusters have been proposed in et al. [13] and Pugia et al. [14,15], which exploit the localized evaporation of a thin water film obtained using micro-engineered surfaces.

Concerning applied materials and manufacturing, Karthikeyan et al. [16] and Cheah and Low [17] proposed two different ceramic MEMS VLMs as an alternative to Si-based VLMs i.e., the low-temperature co-fired temperature ceramic and high resolution in pattern transfer compared to silicon-based MEMS technology, thus prohibiting better manufacturing flexibility and micro-electrical system integration capability to date. Recently, Wang et al. [18] proposed the first prototype of additively manufactured vaporizing liquid microthruster, which was 3D printed using the transparent resin with heat resistance up to 320 °C. The maximum measured thrust was about 740 μN at 2 μL/s water flow rate, giving a specific impulse of 37.7 s.

In VLMs, the water flow is typically heated to temperatures higher than its boiling point. This results in an inherently unstable behavior due to flow boiling instabilities reducing the VLM's lifetime and significantly impairing its nominal performance due to low thermal efficiency and thrust unsteadiness [19]. These boiling instabilities generally occur inside the inlet and heating chambers, causing pressure, temperature, and mass flow rate oscillations, dramatically affecting the expansion process into the micronozzle and hence the propulsive performance. Chen et al. [20] first characterized the two-phase flow in a single-channel silicon-based VLM, observing four different flow patterns, i.e. snake flow, vapor-droplet flow, vapor-droplet-jet flow, and vapor flow. They observed that the snake flow pattern leads to the device failure without proper heating. Instead, Cen and Xu [21] first fabricated a MEMS-based VLM made by parallel microchannels and clearly detected the inception of parallel channel flow boiling instabilities due to explosive boiling. Recently, Kwan et al. [22] developed a VLM operating above the critical heat flux condition in the Leidenfrost boiling regime. To control such flow boiling instability, a novel MEMS-based VLM was designed and manufactured using eight parallel microchannels as a heating chamber equipped with temperature and vapor quality micro-sensors and in-channel secondary low-power resistive heating [23]. Preliminary investigations [24] highlighted the presence of three main flow regimes: fully liquid flow, two-phase flow and fully vaporized flow regimes. The last one was characterized by the establishment of an electro-thermal cycle when operating under direct current (DC) voltage control due to the interaction between temperature, heat flux, vapor content and the temperature-dependent main heater resistance. Furthermore, the rapid modification of the heat transfer coefficient quickly led to the device failure due to excessive thermal stress caused by the boiling crisis. These findings suggested the need for more advanced real-time control of the heat transfer process for flow boiling instability hindering and safe thermal management. The present work shows the first advancements in developing a pulsed heating system actively controlled by temperature instead of by electrical power. In particular, Section 2 presents the description of such a temperature-controlled heating system, which has been built to operate with both manual and data-driven (DD) adaptive [25,26] PI-D control logic. Results are discussed in Section 3, structured into two parts: power consumption assessment in steady-state operation and dynamic response analysis of the VLM using both manual and DD offline adaptive PI-D temperature controls. Finally, the concluding remarks and future steps are outlined in Section 4. The novelty of the present work is summarized as follows:

- A temperature-controlled pulsed heating system based on PI-D logic is implemented in a MEMS VLM for the first time.
- The experimental assessment of the steady-state operation and the dynamic response of the VLM undergoing pulsed heating control is provided by using both manual and data-driven offline adaptive PI-D temperature controls.

2. Experimental method and methodology

2.1. Device description and experimental setup

The VLM has been designed and manufactured by the Institute for Micro-electronics and Micro-systems of the Italian National Research

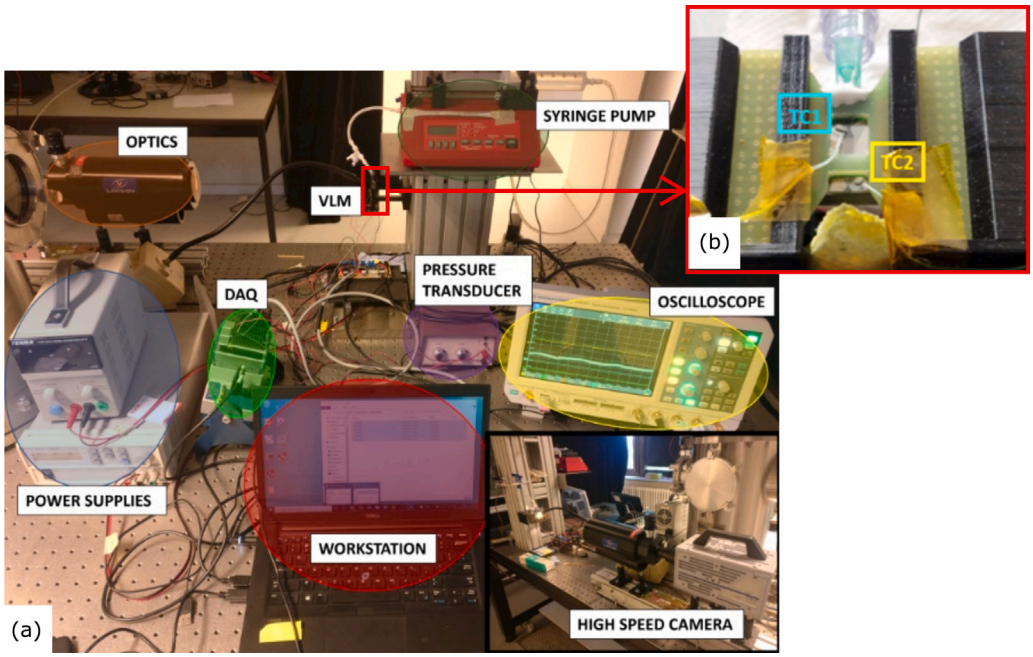

Fig. 1. Experimental setup: (a) overall physical arrangement; (b) VLM configuration with thermocouples TC1 (VLM inlet, cold side) and TC2 (micronozzle entrance, hot side).

Council (CNR-IMM) in collaboration with the Aerospace Propulsion group of the University of Salento (Italy) and the Heat and Mass Transfer group of the KU Leuven (Belgium). The VLM geometry consists of an inlet chamber (rectangular or v-shaped), eight parallel microchannels as a heating chamber, and a tronco-conical planar micronozzle, having an etching depth equal to 230 µm. The CNR-IMM manufactured the VLM using MEMS technology involving RIE, plasma-enhanced chemical vapor deposition, adhesive bonding, micro-alignment, and micro-machining. At the end of the manufacturing process, the VLM structure presents a stacked configuration consisting of a silicon substrate with fluidic structures and a borosilicate glass cover lid. As previously described in [23], the VLM is equipped with seven resistance temperature detectors (RTDs), two arrays of in-channel capacitive void fraction sensors, and in-channel secondary resistive micro-heaters. This microelectronics is deposited on the glass substrate, allowing optical access into the device for flow diagnostics. A specially patterned glue layer binds the silicon and glass substrates and ensures fluid tightness. The VLM was designed to operate with liquid water as propellant, with nominal operating conditions defined as follows:

- mass flow rate ranging between 2.0 and 7.0×10^{-6} kg/s;
- maximum vapor temperature ranging between 150 °C and 300 °C;
- feeding pressure ranging between 10^5 Pa and 2.0×10^5 Pa.

with preliminary estimations of the nominal thrust and specific impulse of 1 mN and 10 mN for the former and 90 s – 110 s for the latter.

The overall experimental setup is depicted in Fig. 1, along with the VLM, equipped with temperature sensors and its water injection system. This one consists of a syringe pump (model NE-1000), a rigid polyvinylchloride (PVC) 50 ml syringe, soft PVC tubing, micro-fluidic valves, and fittings type Luer lock. The feeding pressure and temperature were measured using a relative pressure transducer Validyne DP15 (user calibrated in the relative pressure range 0 bar – 5 bar) and a K-type thermocouple, respectively. Both were located along the water feeding line before the VLM injection system. Concerning the heating system, a DC power supplier (model Agilent 5751a) was electrically connected to the main heater of the VLM through a metal–oxide–semiconductor field-effect transistor (MOSFET), model ICQUANZX, which operated a pulse width modulation (PWM) switch (maximum frequency equal to 20 kHz) allowing for a controlled power gating. The linear Hall effect current sensor HiLetgo ACS758LCB-050B-PFF-T (measuring range: 0 A – 50 A; response time: 16 µs; bandwidth: 120 kHz), placed between the MOSFET and the VLM heater, produced a voltage output which was directly acquired by the oscilloscope R&S RTB2004 (bandwidth: 300 MHz; 4 channels; sampling speed: 1.25 GS/s) using a voltage probe with attenuation factor 1:1. Two voltage probes (attenuation factor 1:1) located on the positive and negative leads of the VLM heater were used to read and record both the applied voltage and the current signals across the VLM main heater. Mounted on a 4-slot chassis NI cDAQ-9174, the module NI-9401 controlled the MOSFET gate by generating the PWM signal. The actively controlled pulsed heating system was linked to the device's temperature readings, obtained from two K-type thermocouples installed on the external surface of the quartz substrate. Fig. 1(b) shows the final configuration of the VLM during testing: TC1 is the thermocouple placed close to the inlet section (cold side), and TC2 is the thermocouple placed close to the micronozzle entrance (hot side). Their signals were acquired using the data acquisition module NI-9211 (sampling speed: 14 Hz aggregate; 4 channels), mounted on the shared data acquisition chassis. This limited the speed of the resulting temperature controller to 4 Hz. The software development of the control system was performed using the toolbox Labview 2018 of National Instruments.

2.2. VLM systems under pulsed heating: an unknown nonlinear plant governing the overall heat transfer process

A theoretical equation of the overall heat transfer process $oHTP(t)$ occurring in a VLM can be derived by equating the total Joule heating produced by the resistive heater $\dot{Q}_R$ (Eq. (1a)) and the total power supplied to the liquid flow to boil and evaporate $\dot{Q}_H$ (Eq. (1b)) without accounting for heat losses.

$$\dot{Q}_R = \frac{V_{max}^2}{R_{MH}(t)} DC^2(t) \tag{1a}$$

$$\dot{Q}_H = \dot{m}\, oHTP(t)\, [T_c(t) - T_{f,i}] \tag{1b}$$

In the equations above, t is the time, V_{max} is the maximum amplitude of the supplied voltage, $\dot{m}$ is the mass flow rate, $T_{f,i}$ is the initial temperature of the fluid at the VLM entrance. The duty cycle $DC(t)$

is related to the pulse width W_{pulse} and the pulse frequency f_{pulse} as $DC(t) = W_{pulse}(t)f_{pulse}$: together with V_{max}, they define the pulsed control space. $R_{MH}(t)$ denotes the electrical resistivity of the heater, which is supposed to linearly depend to the controlled temperature $T_c(t)$ as $R_{MH}(t) = A_{MH} + B_{MH}T_c(t)$. By coupling Eqs. (1a) and (1b), the master equation of the VLM undergoing pulse heating is obtained as follows:

$$B_{MH}T_c^2(t) + [A_{MH} - B_{MH}T_{f,i}]T_c(t) = V_{max}^2 \frac{DC^2(t)}{\dot{m}\, oHTP(t)} + A_{MH}T_{f,i} \quad (2)$$

Eq. (2) outlines the second-order and nonlinear nature of the VLM system. Also, it is characterized by an unknown $oHTP(t)$ due to the complex nature of the two-phase flow, which is governed by local micro- and nano-scale phenomena severely depending on the operating conditions, the VLM geometry, the fluid and solid properties, etc. It is worth outlining that $T_c(t)$ is the control output, $\dot{Q}_R(t)$ is the control action defined by the actuation parameters V_{max}, f_{pulse} and $DC(t)$ (or $W_{pulse}(t)$). In this work, V_{max} and f_{pulse} are preset during control; therefore, the control action is directly driven by $DC(t)$.

2.3. Active pulsed heating using PID control

As demonstrated in [24], a power-controlled system can result in low-frequency oscillations due to the temperature dependence of the heater's resistance and the emergence of a thermo-electric-hydraulic coupling. This highlights the potential benefits of using temperature-based control of the heating system to prevent such instabilities. To achieve this, an effective control system is required to ensure stable operation and minimize detrimental oscillations in pressure and temperature. The Proportional–Integral–Derivative (PID) control system is one of the most widely used in industrial applications [27–31]. The effectiveness of the control system relies on the selection of the appropriate parameters, such as the proportional gain K_P, the integral time T_I, and the derivative T_D time. However, in practice, some modifications are made to the basic form to enhance control performance. One such modification is to avoid the "derivative kick" problem, which is caused by the error signal experiencing a discontinuous step when the setpoint is changed. This can cause an infinite output to the plant. To avoid this problem, the derivative of the output signal is used instead of the error signal. This way, when the reference signal changes, the derivative term is not affected. This implementation is also known as PI-D control. The modified block diagram is shown in Fig. 2(a).

Determining the system's parameters can be achieved by referencing the desired response, assuming the dynamic system model is known. However, in the case of the VLM, the model is not known. Due to its complex heat transfer characteristics and small scale, approximate empirical models are the only means to describe the system's overall behavior. As a result, alternative tuning methods must be considered. These methods are compared based on three key characteristics of the step response: rise time (τ_{rise}), settling time (τ_{set}), and percent overshoot ($\%OS$). Rise time is defined as the duration required for the temperature to increase from 10% to 90% of the step value. Settling time is the duration from initiation of the step until the temperature becomes stable within an error band of 3%. Finally, the percent overshoot is the percentage that the signal exceeds the setpoint.

All post-processing tasks were carried out using user-defined routines that utilized the Matlab toolbox. A trade-off between the parameters is usually required since the response with a low rise time tends to have a significant overshoot. This is a direct consequence of the choice of PID parameters. In this regard, the classical heuristic approach of Ziegler–Nichols [32] easily identifies the PID parameters, yet their values can result far from the optimum. The Ziegler–Nichols method involves setting the integral and derivative terms to zero and gradually increasing the proportional gain until stable oscillations are observed in the output. If the gain was increased even more from this point, the oscillations should increase and become unstable. This value for the proportional gain is called the ultimate gain K_u. The period of oscillations corresponding to the ultimate gain is called the ultimate period T_u. Therefore, the PID parameters are computed based on the ultimate gain and period.

Heuristic tuning methods such as Ziegler–Nichols tuning are challenging to apply to nonlinear systems, as is the case for the VLM. A manual tuning approach can be a more effective alternative, in which the user adjusts parameters through trial-and-error and directly observes the resulting response. Ideally, the output should exhibit minimal overshoot and rise time while also having a short settling time. The parameters cannot, however, all be optimized at the same time. Thus a trade-off is required while considering what is more important to the application at hand. However, the nonlinear nature of the VLM makes it challenging to achieve adequate control throughout its entire operating range. Due to the impact of the vapor content on the heat transfer characteristics, the temperature response to a change in controller output can vary significantly depending on the flow regime. Consequently, adaptive capabilities in setting the PID parameters are required to achieve optimal performance based on the flow boiling regime: for this purpose, the complex and unpredictable behavior of the VLM makes data-driven approaches the most appropriate. Additionally, an adaptive controller can adjust the PID parameters dynamically to better handle the nonlinearity of the system [33]. Artificial intelligence-based algorithms for dynamic tuning PID parameters have been widely preferred in the literature for different systems [34–37]. In the present work, the adaptive DD PI-D controller proposed in [25,26] has been implemented. The block diagram of the adaptive controller is shown in Fig. 2(b), and the adaptive algorithm consists of the following steps. First, the database is created and the data storage function $\mathbf{\Phi}$ is built. It includes an information vector $\phi(t)$ and a control vector $\theta^{PID}(t)$ containing the PID parameters. The information vector consists of the setpoint signal $T_{set,2}(t)$, the system input signal $DC(t)$, and the system output signal $T_{TC2}(t)$. Thus, a data set of size $\mathcal{N}_{DB}$ looks as follows:

$$\mathbf{\Phi}_j = [\phi(\bar{t}_j), \theta^{PID}(\bar{t}_j)], \quad j = 1, 2, \dots \mathcal{N}_{DB} \quad (3)$$

with

$$\begin{aligned}\phi(\bar{t}_j) &= [\phi_1(\bar{t}_j), \phi_2(\bar{t}_j), \phi_3(\bar{t}_j), \phi_4(\bar{t}_j), \phi_5(\bar{t}_j), \phi_6(\bar{t}_j)] \\ &= [T_{set,2}(\bar{t}_j + 1), T_{set,2}(\bar{t}_j), T_{TC,2}(\bar{t}_j - 1), T_{TC2}(\bar{t}_j), DC(\bar{t}_j - 1), DC(\bar{t}_j)]\end{aligned} \quad (4)$$

$$\theta^{PID}(\bar{t}_j) = [K_P(\bar{t}_j), T_I(\bar{t}_j), T_D(\bar{t}_j)] \quad (5)$$

while during the PID control at ith loop occurring at the time t_i (i.e., the current state of the system), the information and the control vectors are:

$$\begin{aligned}\phi(\bar{t}_i) &= [\phi_1(\bar{t}_i), \phi_2(\bar{t}_i), \phi_3(\bar{t}_i), \phi_4(\bar{t}_i), \phi_5(\bar{t}_i), \phi_6(\bar{t}_i)] \\ &= [T_{set,2}(\bar{t}_i + 1), T_{set,2}(\bar{t}_i), T_{TC,2}(\bar{t}_i - 1), T_{TC2}(\bar{t}_i), DC(\bar{t}_i - 1), DC(\bar{t}_i)]\end{aligned} \quad (6)$$

$$\theta^{PID}(\bar{t}_i) = [K_P(\bar{t}_i), T_I(\bar{t}_i), T_D(\bar{t}_i)] \quad (7)$$

The adaptive algorithm compares the current data sample with historical data to determine the best course of action. This is done by calculating the distance between the current and historical data in each iteration. The distances are calculated as follows:

$$d_j(t_i, \bar{t}_j) = \sum_{l=1}^{6} \left| \frac{\phi_l(t_i) - \phi_l(\bar{t}_j)}{\max\limits_{k \le \mathcal{N}_{DB}} \{\phi_l(\bar{t}_k)\} - \min\limits_{k \le \mathcal{N}_{DB}} \{\phi_l(\bar{t}_k)\}} \right| \quad (8)$$

with j the number of data sets in the database the length of the information vector. The denominator in Eq. (8) represents the difference between the maximum and minimum values of the lth element of all data sets in the database. In the final step, the distances are sorted in ascending order, and weights are calculated based on a selection

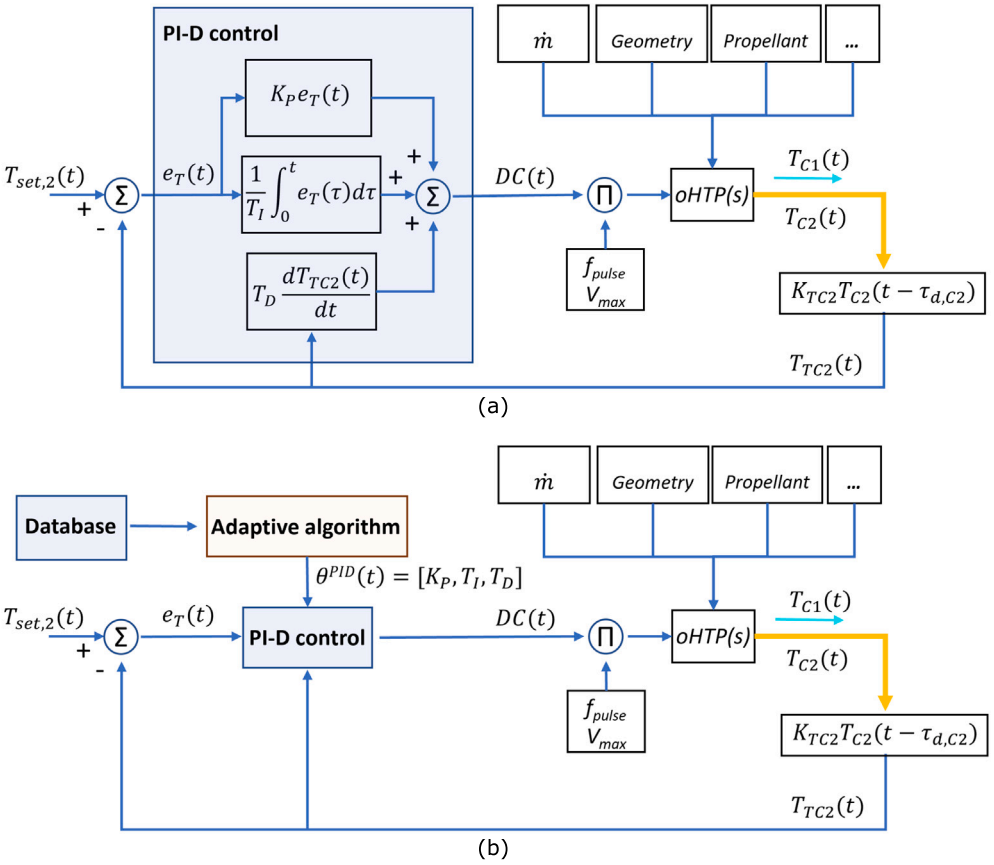

Fig. 2. Block diagrams of the PID controllers: (a) PI-D controller; (b) data-driven adaptive PID controller.

of the smallest distances according to Eq. (9) with the N_w selected distances. The smaller the distance, the larger the weight assigned to the corresponding data set.

$$w_n(t_i, \bar{t}_j) = \frac{\exp(-d_n(t_i, \bar{t}_n))}{\sum_{m=1}^{N_w} \exp(-d_m(t_i, \bar{t}_m))} \quad n = 1, 2, \ldots N_w \tag{9}$$

New PID parameters are then calculated as shown in Eq. (10) by taking the weighted sum.

$$\theta^{PID}(t_i) = \sum_{n=1}^{N_w} w_n(t_i, \bar{t}_n) \cdot \theta^{PID}(\bar{t}_n) \tag{10}$$

It is worth observing that in such adaptive control, the data stored in the database is crucial for the appropriate functioning of the controller since the algorithm itself is not designed to correct badly tuned parameters.

3. Results and discussion

This section presents the results of the VLM's heat transfer analysis under pulsed heating control, which is divided into two parts: the assessment of power consumption during steady-state operation (Section 3.1) and the analysis of the VLM's dynamic response using both manual and DD offline adaptive PI-D temperature controls (Section 3.2).

3.1. Effect of the pulsed heating on VLM power consumption in steady-state operation

The experimental evaluation of the VLM's power consumption P_d under pulsed heating during steady-state operation (average fluctuation of T_{TC2} with respect to T_{set} within an error band of 3%, i.e. $|T_{TC2} - T_{set}| < 0.03\ T_{set}$) is discussed below. In such conditions, a number $N_{pulse} = 3$ of synchronized electrical signals (applied voltage $V(t)$ and current $I(t)$) have been acquired using the oscilloscope. Fig. 3 shows an example of the applied voltage pulse and the resulting current pulse acquired during steady-state operation at $\dot{m}$ = 10 ml/h, f_{pulse} = 1000 Hz, V_{max} = 10 V and T_{set} = 100 °C.

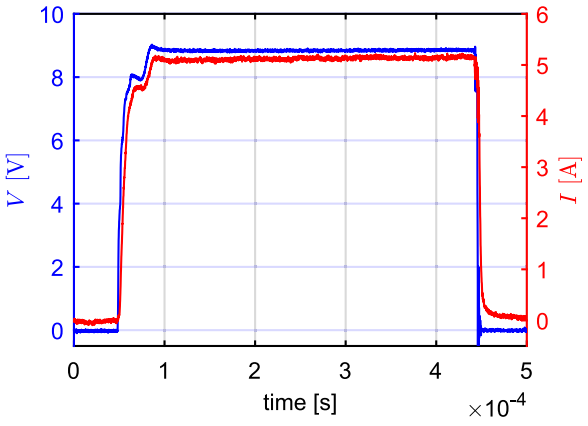

Fig. 3. Applied voltage and current pulses at $\dot{m}$= 10 ml/h, f_{pulse} = 1000 Hz, V_{max} = 10 V and T_{set} = 100 °C.

At each operating condition with a given $\dot{m}$, V_{max}, f_{pulse}, and T_{set}, the average power $P_{d,avg}$ results then as follows:

$$P_{d,avg} = \frac{1}{N_{pulse}} f_{pulse} \sum_{i=1}^{N_{pulse}} \int_0^{t_{pulse,i}} V_i(t) I_i(t) dt \tag{11}$$

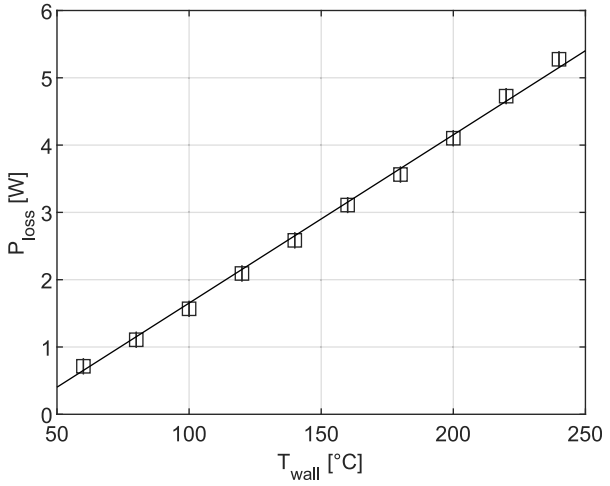

Fig. 4. Power losses P_{loss} to the surroundings due to conduction, convection, and radiation.

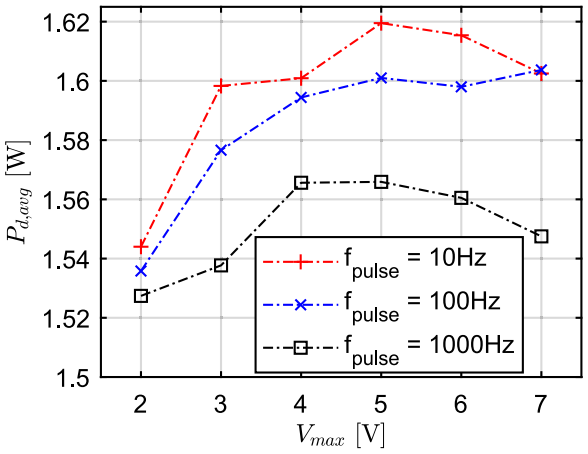

Fig. 5. Power consumption in dry conditions for different pulse frequencies at T_{set} = 100 °C. Unbiased standard deviation of the power consumption $\sigma_{Pd,max}$: 0.012 W at 10 Hz, 0.03 W at 100 Hz, and 0.05 W at 1000 Hz.

with unbiased standard deviation σ_{Pd} equal to

$$\sigma_{Pd} = \sqrt{\frac{1}{N_{pulse}} \sum_{i=1}^{N_{pulse}} \left[f_{pulse} \int_0^{t_{pulse,i}} V_i(t) I_i(t) dt - P_{d,avg} \right]} \tag{12}$$

Based on the average power consumption, the VLM heating efficiency $\eta_{heating}$ is computed using the ideal power P_{ideal} and the estimation of the dry losses P_{loss} (see Eq. (13)).

$$\eta_{heating} = \frac{P_{ideal}}{P_{d,avg} - P_{loss}} \tag{13}$$

In the equation above, P_{ideal} is given by the sum of the enthalpy required to heat the liquid to saturation temperature, the enthalpy of vaporization, and the enthalpy for overheating the vapor up to the setpoint temperature (see Eq. (14)). Furthermore, the thermophysical properties of the fluid, viz. the specific heat at a constant pressure of both liquid phase $c_{p,l}$ and vapor phase $c_{p,v}$, the saturation temperature T_{sat} at the measured inlet pressure p_{inlet}, and the latent heat of vaporization h_L, are retrieved using the thermophysical property database CoolProp [38].

$$P_{ideal} = \dot{m} \left[c_{p,l}(T_{sat} - T_{f,i}) + h_L + c_{p,v}(T_{set} - T_{sat}) \right] \tag{14}$$

Power measurements obtained under dry conditions have been used to estimate the heat losses (conduction, convection, and to a lesser extent, radiation) to the surroundings, as shown in Fig. 4: Eq. (15) relates the resulting P_{loss} [W] as a function of the measured temperature T_{TC} in °C.

$$P_{loss} = 0.025\, T_{TC} - 0.8474 \quad (R^2 = 0.9973) \tag{15}$$

In this way, the heating efficiency $\eta_{heating}$ provides a measure of the energy transfer losses due to the thermodynamic irreversibilities occurring during the overall heating process.

Power consumption analysis in dry conditions. The present analysis is based on tests performed in dry conditions at T_{set} = 100 °C by varying the f_{pulse} from 10 Hz to 1000 Hz and increasing V_{max} from 2 V to 7 V by steps of 1 V. For each voltage and pulse frequency setting, the parameters of the PI-D temperature controller have been manually adjusted to keep the temperature as stable and close as possible to the setpoint temperature. Therefore, for a given f_{pulse}, the more V_{max} increases, the lower $DC(t)$ results. Fig. 5 shows the average power consumption, with $\sigma_{Pd,max}$ equal to 0.012 W at 10 Hz, 0.03 W at 100 Hz, and 0.05 W at 1000 Hz. It is evinced that the smaller f_{pulse} and $DC(t)$ are, the larger the power required to keep the temperature at 100 °C becomes, with an average power consumption almost 2.5% lower at 1000 Hz than at 10 Hz. Such a frequency effect reduces by increasing $DC(t)$, as the time the heating is off reduces too, no matter the frequency. A high pulse frequency with a low voltage setting in dry conditions is beneficial since the low voltage setting results in a high-duty cycle, decreasing the required power. However, for control purposes, this is not suitable as a higher voltage setting is desired to avoid duty cycle saturation at high-temperature setpoints and ensure faster control.

Power consumption analysis with liquid feeding. The power consumption analysis with liquid feeding has been performed at fixed V_{max} = 10 V, f_{pulse} = 1000 Hz and operating temperature ranging from 120 °C to 180 °C with incremental steps of 20 °C. Three different mass flow rates have been investigated, i.e., $\dot{m}$ equal to 10 ml/h, 18 ml/h and 24 ml/h. Fig. 6 shows a typical temporal evolution of the measured signals during testing: the inlet temperature T_{TC1}, the (controlled) nozzle temperature T_{TC2}, the setpoint temperature T_{set} and the average device temperature $T_{avg} = 0.5(T_{TC1} + T_{TC2})$. It is worth underlining the manual in-running tuning of the PID parameters K_P, T_I, and T_D operated to keep the temperature stable and close to the setpoint temperature, with maximum power fluctuations $\sigma_{Pd,max}$ equal to 0.56 W.

Fig. 7 illustrates the average power consumption and the heating efficiency as a function of the setpoint temperature for each mass flow rate. The heat losses have been calculated using T_{avg} in Eq. (13), due to the significant difference between T_{TC2} (hot side) and T_{TC1} (cold side).

The best performances occur at $\dot{m}$ = 18 ml/h, where a linear increase of the power consumption $P_{d,avg}$ is observed in the range of 120 °C – 160 °C. According to the $P_{d,avg}$, $\eta_{heating}$ also increases linearly from 120 °C to 160 °C, with maximum heating efficiency equal to about 94%. This increase of the average efficiency couples with more effective control of the flow boiling oscillations, as confirmed by the reduction of the standard deviation of both $P_{d,avg}$ and $\eta_{heating}$. However, at 180 °C, the efficiency decreased due to the nonlinear increase in average power consumption, presumably due to the establishment of an extended annular flow regime within the VLM, which also reduces the average heating efficiency. By increasing the mass flow rate at 24 ml/h, the linear dependency between $\eta_{heating}$ and T_{set} is lost, and the performance gets slightly worse, suggesting a less effective control of the faster flow boiling regime. However, these results confirm that a pulsed heating strategy can significantly enhance heating efficiency from the typical value of 0.55 [24] to values above 0.9. Working at the lowest mass flow rate, the heating process becomes significantly less efficient, with $\eta_{heating}$ approaching 0.8 as increasing T_{set}. The main reason behind such

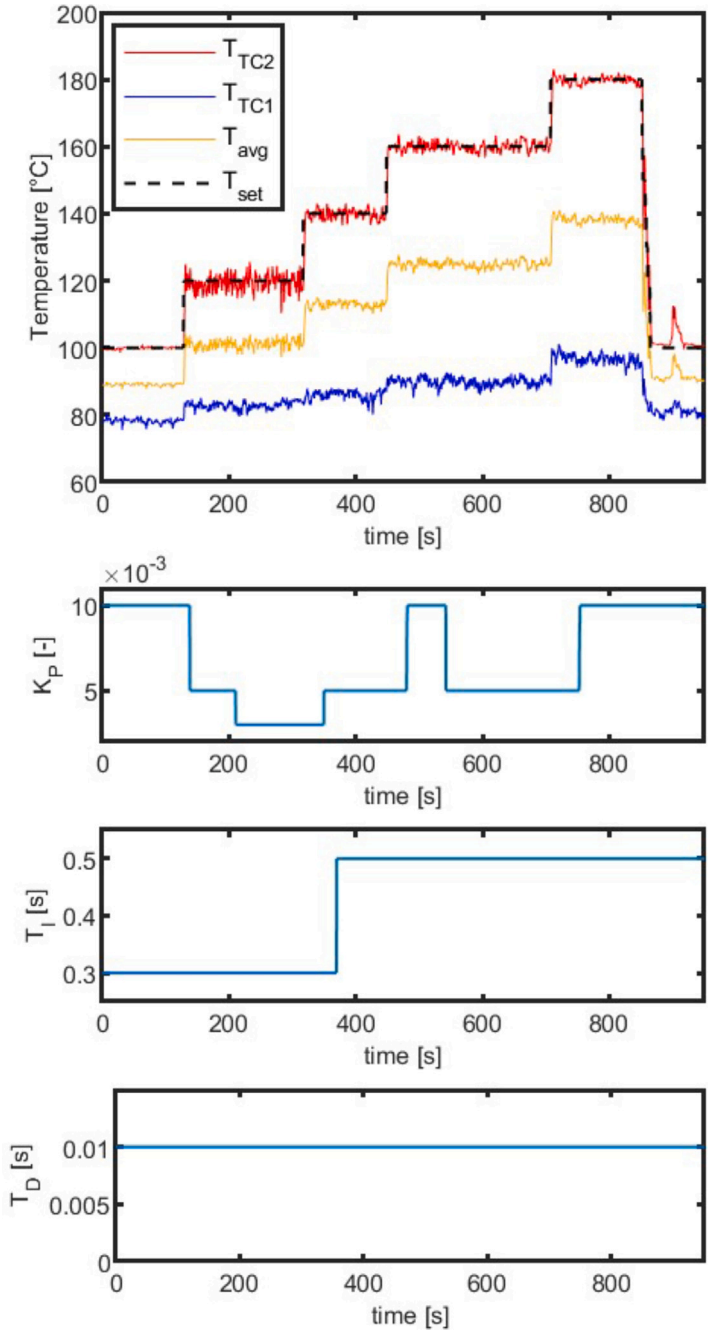

Fig. 6. Power consumption analysis with liquid feeding: temporal signals of the inlet temperature T_{TC1}, nozzle temperature T_{TC2}, average temperature T_{avg}, PID parameters K_P, T_I and T_D.

an efficiency loss is the slower flow, which triggers stronger explosive boiling phenomena in the inlet chamber and severe flow reversal into microchannels, causing more prominent flow maldistribution along microchannels and, hence, mass flow rate oscillations.

3.2. Dynamic temperature control using pulsed heating

The spacecraft attitude control system may require a specific thrust temporal profile, which can be attained by changing the setpoint temperature of the thruster. Therefore, besides steady-state stability, the temperature also needs to be able to efficiently follow setpoint changes. Thus, to maximize the performance of the attitude control system, the vaporization and heat transfer process optimization during step response transients becomes a key aspect. In addition, thermal stresses are the primary source of device failure during transient set-point changes due to the fast local deterioration of the heat transfer coefficient coupled with severe heat flux gradients and the modification of the flow boiling regimes. In this regard, thermal stresses certainly concentrate at the interface between various substrates of dissimilar materials owning different thermal behaviors. The following sections present the assessment of the dynamic response using the PI-D controller with three different tunings, i.e., the classical Ziegler–Nichols method, manual tuning with fixed PID parameters, and the data-driven adaptive method. Experiments were carried out at the same pulse

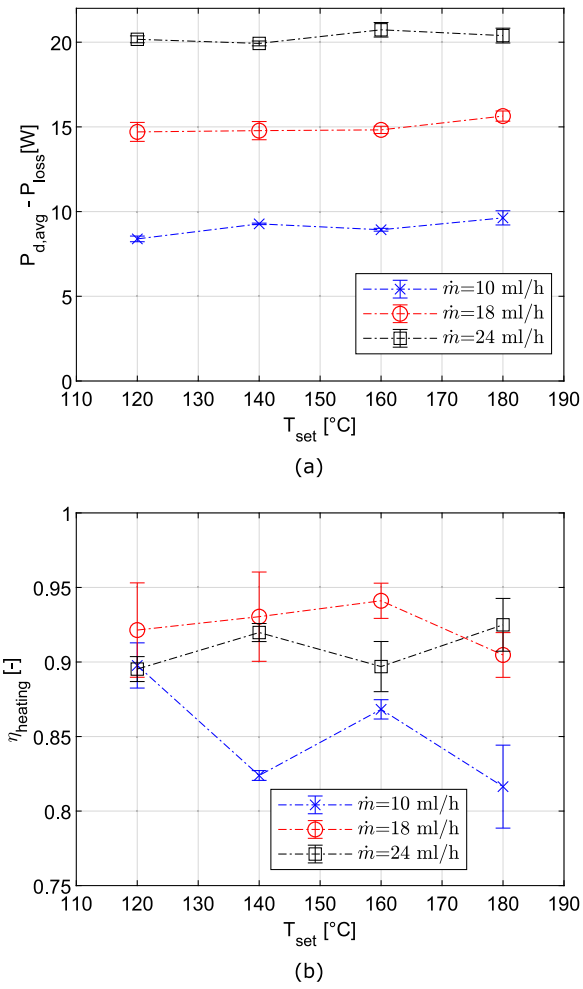

Fig. 7. Power consumption analysis with liquid feeding: (a) ideal power consumption, measured power consumption and heat losses, (b) heating efficiency.

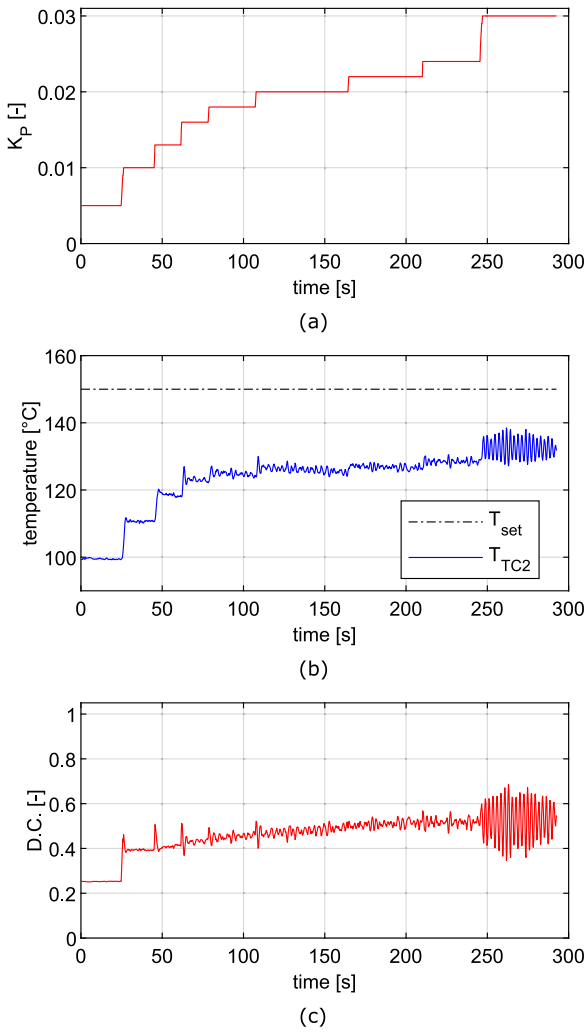

Fig. 8. Ziegler–Nichols method: ultimate gain analysis.

Table 1
Ziegler–Nichols method: results.

	PI	PID
K_P [–]	0.45 K_u = 0.0135	0.6 K_u = 0.018
T_I [s]	0.8 T_u = 1.8	1.5 T_u = 0.1.125
T_D [s]	0	0.125 T_u = 0.03125

frequency and mass flow rate as in the previous steady-state analysis, i.e., f_{pulse} = 1000 Hz and $\dot{m}$= 18 ml/h.

Ziegler–nichols and manual tuning with fixed PID parameters. According to the heuristic rules by Ziegler and Nichols, the integral and derivative actions of the controller are set to zero, and the proportional gain is stepwise increased. When applied to the VLM control, T_{set} and V_{max} have been fixed at 150 °C and 8 V, respectively. The resulting tuning process is shown in Fig. 8.

The beginning of the temperature oscillation indicates that the ultimate gain K_u is reached. Thus, K_u and the corresponding ultimate oscillation period T_u, allow setting the PID parameters via the heuristic rules reported in Table 1. In our test, it resulted in K_u = 0.03 and T_u = 2.25 s.

As shown in Fig. 9, the PI parameters give a very slow response with a settling time of almost 100 s, which is unsuitable for VLM applications. On the other hand, when using the calculated PID gains, minor errors in the controller input are easily amplified to overly high control action. Consequently, even without modifying the setpoint temperature, the system is prone to become unstable with unwanted and uncontrolled oscillations, as shown in Fig. 10. In conclusion, the nonlinear behavior of the VLM shows to be not compatible with the Ziegler–Nichols method, and another way of tuning is required.

To minimize rise time, settling time, and overshoot, one can manually adjust the PID gains using a trial-and-error approach. This tuning method requires considerable work to find the appropriate parameters for every operating condition, setpoint temperature, and V_{max}-f_{pulse} combination. The best trade-off (based on the operator experience) between the VLM response performance among all the investigated PID settings was retrieved in the following ones:

$$K_P = 0.014, T_I = 0.25\,\text{s}, T_D = 0.01\,\text{s}$$

As shown in Figs. 11 and 12 and reported in Table 2, using those parameters, the heating control is enhanced and more effective. However, manual tuning remains a trial-and-error approach which is very sensitive to the operator experience, the operating conditions, and the reference temperature profile. Therefore, this approach is also unsuitable for VLM operations. Still, it can be used to build a dataset of the dynamic response of the VLM for more advanced data-driven controls.

Data-driven offline adaptive method. An adaptive method adjusts the PID parameters dynamically by using a predictive model of the system or by referencing a database of responses obtained from multiple tests with various fixed gains, also known as system training. This database

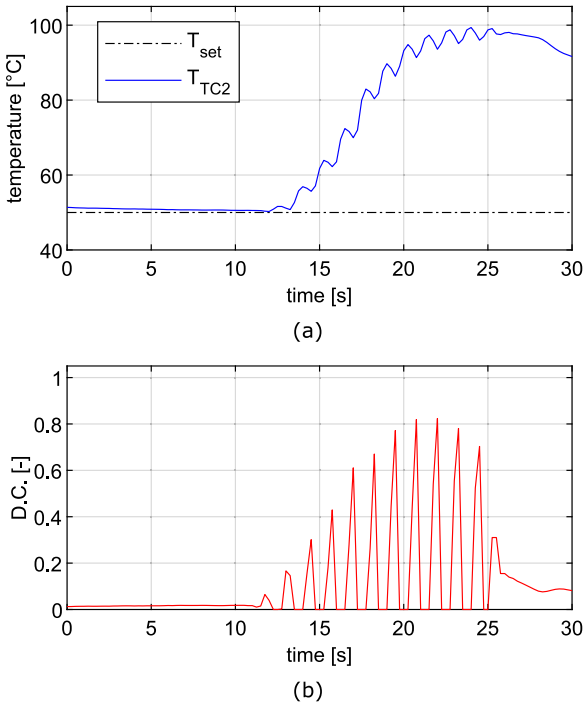

Fig. 9. Ziegler–Nichols method: PI step response.

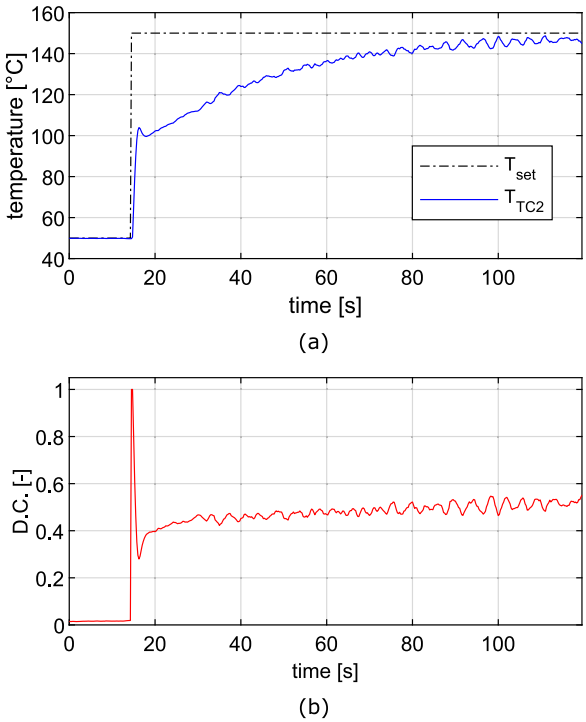

Fig. 10. Ziegler–Nichols method: PI-D step response.

represents the system's "experience" and the foundation of the data-driven methods. In this study, this approach is selected due to the nonlinear nature of the VLM system, whose plant functions are also unknown. In our methodology, the training occurred once, as the initial step of the overall procedure described in Section 2.3 and shown in Fig. 2. Consequently, the resulting tuning method is a data-driven offline adaptive method. The first step was thus building the database,

Table 2
Dynamic response analysis with manual tuning with fixed PID parameters.

Text #	K_P [−]	T_I [s]	T_D [s]	τ_{rise} [s]	τ_{set} [s]	$\%OS$ [−]
MT1	0.0072	0.12	0.010	2.55	31.25	14.95
MT2	0.0102	0.20	0.001	2.99	21.23	–

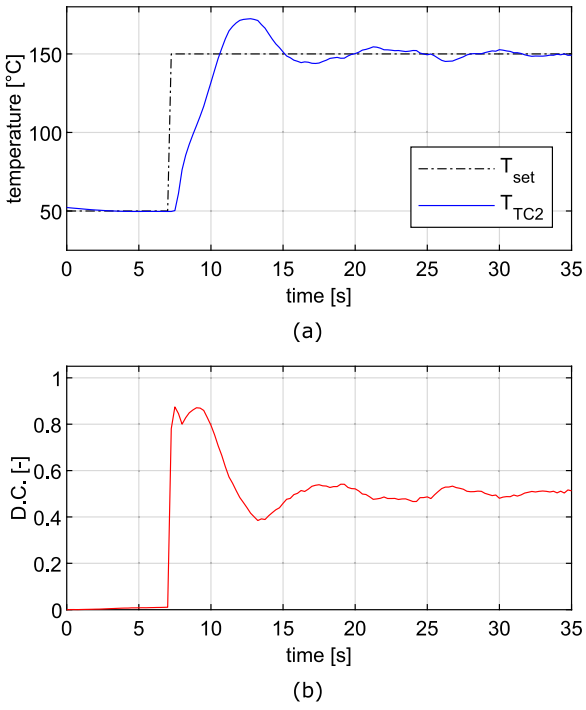

Fig. 11. Dynamic response with manual tuning with fixed PID parameters: test case MT1.

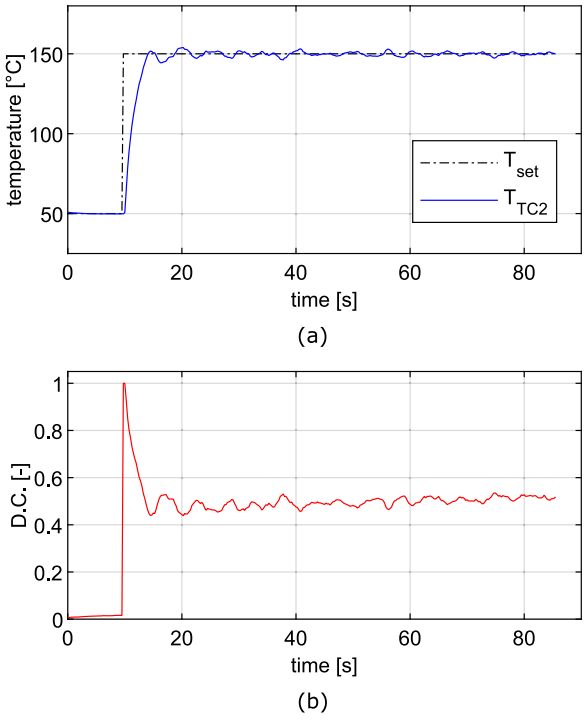

Fig. 12. Dynamic response with manual tuning with fixed PID parameters: test case MT2.

Table 3
Adaptive data-driven PID control: step response database.

ΔT_{step} [°C]	K_P [−]	T_I [s]	T_D [s]
50–180	0.015	0.30	0.01
50–100	0.020	0.08	0.01
50–110	0.014	0.14	0.02
50–150	0.014	0.25	0.01
50–180	0.025	0.20	0.03

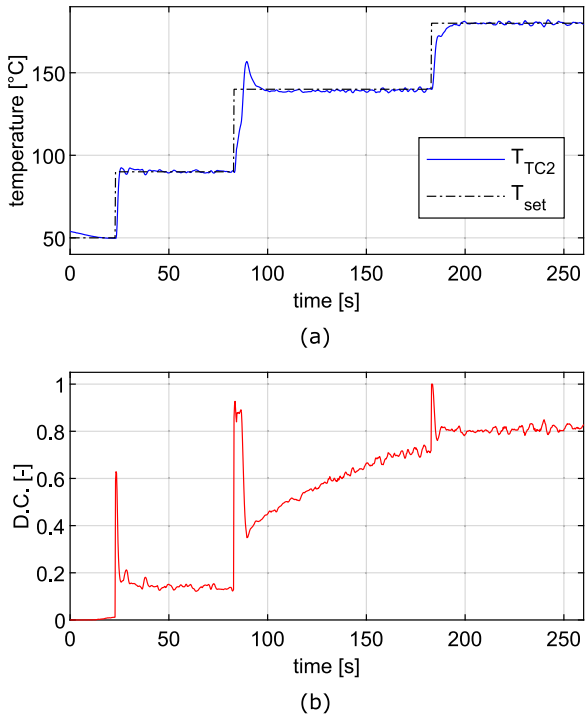

Fig. 13. Dynamic step response using fixed PID control (K_P = 0.014; T_I = 0.25 s; T_D = 0.01 s).

and the manual tuning process has been demonstrated to be an effective way to do so. It is worth observing that the data can be appropriately chosen to reduce the database size while ensuring adequate experience. The most straightforward way is to add step responses for each flow regime so that the controller can adapt its parameters to it. However, that still leaves many options regarding how to build the experience of the system. In the present work, the adaptive controller is based on the consecutive step responses at fixed PID parameters reported in Table 3, which experienced the system over the different flow boiling regimes. A preliminary analysis highlighted no significant enhancement when using numbers of selected distances higher than 20; thus, the number of selected distances N_w was set to 20.

The comparison of the response characteristics between the dynamic response under DD adaptive PID control and manually tuned fixed PID parameters is presented in Table 3.

As confirmed in Fig. 13, the fixed controller exhibited increasing rise and settling times as a function of the setpoint temperature, with maximum τ_{rise} and T_{set} equal to 6.35 s and even about 1 min, respectively. Furthermore, a relatively high overshoot of about 12% occurred when crossing the saturation temperature at T_{set} = 140 °C. The proportional gain and increases with larger temperature steps

Table 4
Dynamic response analysis: comparison fixed PID control (K_P = 0.014; T_I = 0.25 s; T_D = 0.01 s) vs DD adaptive PID control.

PID controller	T_{set} [°C]	τ_{rise} [s]	τ_{set} [s]	$\%OS$ [−]
Fixed	90	1.15	8.08	2.72
	140	3.73	11.09	12.02
	180	6.35	59.36	1.16
Adaptive	90	1.70	2.80	2.11
	140	3.08	3.35	0
	180	3.25	9.17	2.33

primarily cause overshoot. To mitigate this effect, an intermediate step of 140 °C may be implemented, though it also prolongs the response time. This highlights the nonlinear nature of the system, which cannot be effectively addressed using fixed PID parameters alone.

Fig. 14(a) shows the VLM response using the data-driven adaptive controller. Enhanced control authority is found above the saturation conditions with respect to using fixed PID parameters: rise time and settling time are considerably reduced, and the overshoot at 140 °C is not experienced, as evinced in Table 4. A slight disturbance is observed at T_{set} = 140 °C and about 109 s, presumably due to occurrence of a flow boiling instability which was immediately controlled. Fig. 14(b) illustrates the temporal evolution of the PID parameters during the test. In this regard, when the setpoint changes, the parameters adapt as well; when the setpoint is fixed, the parameters remain mostly stable, as expected when the steady-state operation is reached.

Finally, it is worth noting that the performance of the data-driven adaptive control strictly depends on the database training: the more reliable the system experience is, the higher the supervisory authority becomes.

4. Conclusions

A water-fed MEMS vaporizing liquid microthruster has been designed and fabricated. This study provides a comprehensive and detailed experimental evaluation of a temperature-controlled pulsed heating system using a PI-D logic applied to the VLM. The performance of the actively controlled pulsed heating was assessed in terms of power consumption during steady-state operation and dynamic response of the VLM using both manual and data-driven offline adaptive PI-D temperature controls. This study reveals a substantial improvement in heating efficiency during steady-state operation, with values rising from 0.55 (previously obtained with power-controlled heating) to above 0.9 using temperature-controlled pulsed heating, reaching a peak of 94% at a setpoint temperature of 160 °C. Furthermore, it is found that the thermal response of the device during fast heating transients requires a more advanced control strategy than a trial-and-error method, as the manual tuning process is highly dependent on the operator's experience, operating conditions and reference temperature profile. For instance, shorter rise and response times require a higher proportional gain, while the overshoot experienced when crossing the saturation temperature cannot be avoided, especially in the presence of faster modification of the setpoint temperature. In the present work, the use of a data-driven adaptive controller largely overcame this issue, reducing the maximum settling time from approximately 59 s to less than 10 s and eliminating overshooting through the dynamic modification of PID parameters. However, it is worth noting that the scope of this investigation was limited to a specific range of operating conditions and control parameters. Future research will involve expanding the analysis to different mass flow rates and voltage settings, as well as incorporating embedded RTDs and secondary heaters to enhance the temperature-based control system's speed and exploring different versions of PID controllers, such as fractional order PID and proportional–integral–derivative–accelerative controllers.

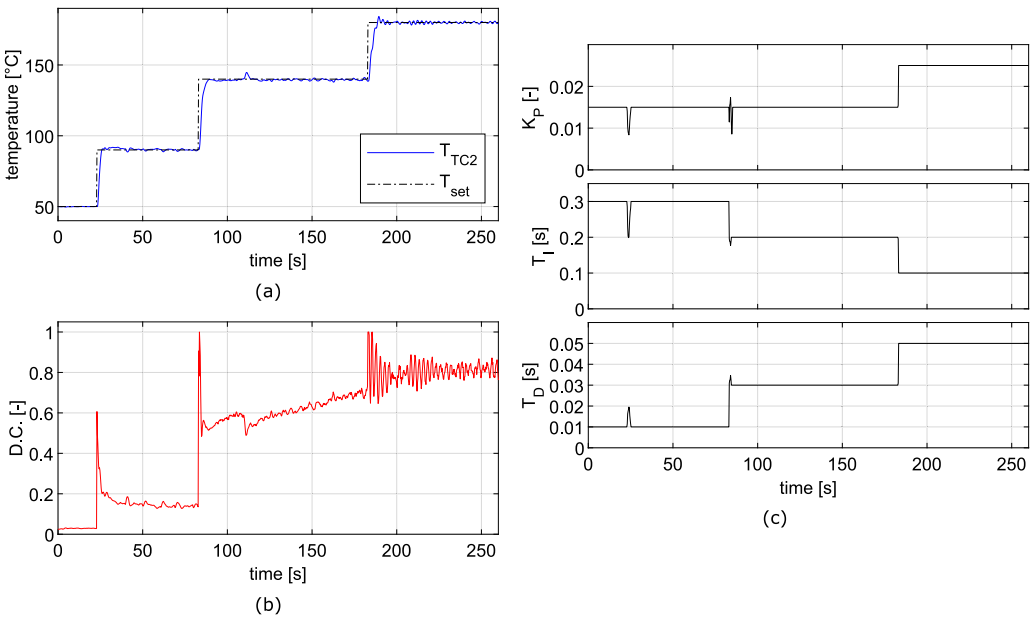

Fig. 14. Dynamic step response using DD adaptive PID control.

Declaration of competing interest

The authors declare that they have no known competing financial interests or personal relationships that could have appeared to influence the work reported in this paper.

Acknowledgments

The authors gratefully acknowledge the financial support of the European Space Agency from the Open Space Innovation Program (OSIP) – Open Discovery Ideas, grant No. 4000 135973/21/NL/GLC/my. Special acknowledgment also to the technical staff of CNR-IMM C. Martucci, A. Campa, P. Cretì, E. Melissano, F. Casino; to A. M. Toscano (Univ. of Salento), H. Van Eyken, and T. Heskens (KU Leuven) for their precious support during the research activities.

References

[1] D.C. Guerrieri, M.A.C. Silva, A. Cervone, E. Gill, Selection and characterization of green propellants for micro-resistojets, J. Heat Transfer 139 (10) (2017) 102001, http://dx.doi.org/10.1115/1.4036619.

[2] J. Mueller, W. Tang, A. Wallace, R. Lawton, W. Li, D. Bame, I. Chakraborty, Design, analysis and fabrication of a Vaporizing Liquid Micro-Thruster, in: 33rd Joint Propulsion Conference and Exhibit, 1997, p. 3054.

[3] J. Mueller, D. Bame, I. Chakraborty, A. Wallace, W. Tang, R. Lawton, Proof-of-concept demonstration of a vaporizing liquid micro-thruster, in: 34th AIAA/ASME/SAE/ASEE Joint Propulsion Conference and Exhibit, 1998, p. 3924.

[4] J. Mueller, I. Chakraborty, D. Bame, W. Tang, Vaporizing liquid microthruster concept: Preliminary results of initial feasibility studies, 2000, pp. 215–230, Micropropulsion for small spacecraft, Reston, VA, American Institute of Aeronautics and Astronautics, Inc.(Progress in Astronautics and Aeronautics, Vol. 187.

[5] Y. Gao, Y.F. Ma, J.T. Liu, A review of the vaporizing liquid microthruster technology, in: 2014 ISFMFE - 6th International Symposium on Fluid Machinery and Fluid Engineering, IET Conference Publications, 2014, pp. 1–3.

[6] E.V. Mukerjee, A.P. Wallace, K.Y. Yan, D.W. Howard, R.L. Smith, S.D. Collins, Vaporizing liquid microthruster, Sensors Actuators A 83 (1) (2000) 231–236, http://dx.doi.org/10.1016/S0924-4247(99)00389-1.

[7] D.K. Maurya, S. Das, S.K. Lahiri, Silicon MEMS vaporizing liquid microthruster with internal microheater, J. Micromech. Microeng. 15 (5) (2005) 966.

[8] P. Kundu, T.K. Bhattacharyya, S. Das, Design, fabrication and performance evaluation of a vaporizing liquid microthruster, J. Micromech. Microeng. 22 (2) (2012) 025016.

[9] X.Y. Ye, F. Tang, H.Q. Ding, Z.Y. Zhou, Study of a vaporizing water micro-thruster, Sensors Actuators A 89 (1–2) (2001) 159–165.

[10] M.A.C. Silva, D.C. Guerrieri, H. van Zeijl, A. Cervone, E. Gill, Vaporizing liquid microthrusters with integrated heaters and temperature measurement, Sensors Actuators A 265 (2017) 261–274.

[11] B. Liu, X. Li, X. Yang, J. Yang, Y. Wang, D. Li, G. Gao, A new vaporizing liquid microthruster with planar induction heating, Sensors Actuators A 308 (2020) 112010, http://dx.doi.org/10.1016/j.sna.2020.112010.

[12] B. Liu, X. Yang, Y. Wang, A tubular vaporizing liquid micro-thruster with induction heating, Heat Mass Transf. 56 (2020) 2035–2043.

[13] A. Sharma, N. Dev, S. Dash, Capillary-fed evaporative microthruster for nano/microsatellites, in: AIAA SCITECH 2022 Forum, 2022, p. 0240.

[14] S.M. Pugia, R.J. Clay, M.F. Fuehne, M.M. Linker, N.C. Franks, B. Davis, K.L. Fowee, Liquid water micropropulsion system for small satellites, in: AIAA Scitech 2019 Forum, 2019, p. 0153.

[15] S. Pugia, A. Cofer, A. Alexeenko, Characterization of film-evaporating micro-capillaries for water-based microthruster, Acta Astronaut. 196 (2022) 442–458, http://dx.doi.org/10.1016/j.actaastro.2020.09.011.

[16] K. Karthikeyan, S. Chou, L. Khoong, Y. Tan, C. Lu, W. Yang, Low temperature co-fired ceramic vaporizing liquid microthruster for microspacecraft applications, Appl. Energy 97 (2012) 577–583.

[17] K.H. Cheah, K.-S. Low, Fabrication and performance evaluation of a high temperature co-fired ceramic vaporizing liquid microthruster, J. Micromech. Microeng. 25 (1) (2015) 015013.

[18] X. Wang, Z. Fei, V.L. Wong, Y. Ren, K.H. Cheah, Additively manufactured vaporizing liquid microthruster with micro pin fins for enhanced heat transfer, Acta Astronaut. 199 (2022) 58–70, http://dx.doi.org/10.1016/j.actaastro.2022.07.001.

[19] D. Fontanarosa, L. Francioso, M.G. De Giorgi, M.R. Vetrano, MEMS vaporazing liquid microthruster: A comprehensive review, Appl. Sci. 11 (19) (2021) http://dx.doi.org/10.3390/app11198954.

[20] C.-C. Chen, C.-W. Liu, H.-C. Kan, L.-H. Hu, G.-S. Chang, M.-C. Cheng, B.-T. Dai, Simulation and experiment research on vaporizing liquid micro-thruster, Sensors Actuators A 157 (1) (2010) 140–149.

[21] J.W. Cen, J.L. Xu, Performance evaluation and flow visualization of a MEMS based vaporizing liquid micro-thruster, Acta Astronaut. 67 (3–4) (2010) 468–482, http://dx.doi.org/10.1016/j.actaastro.2010.04.009.

[22] P.-W. Kwan, X. Huang, X. Zhang, Design and testing of a microelectromechanical-system-based high heat flux vaporizing liquid microthruster, Acta Astronaut. 170 (2020) 719–734, http://dx.doi.org/10.1016/j.actaastro.2020.01.017.

[23] D. Fontanarosa, C. De Pascali, M.G. De Giorgi, P. Siciliano, A. Ficarella, L. Francioso, Fabrication and embedded sensors characterization of a micromachined water-propellant vaporizing liquid microthruster, Appl. Therm. Eng. 188 (2021) 116625, http://dx.doi.org/10.1016/j.applthermaleng.2021.116625.

[24] D. Fontanarosa, L. Francioso, M.G. De Giorgi, C. De Pascali, A. Ficarella, M.R. Vetrano, Flow regime characterization of a silicon-based vaporizing liquid microthruster, Acta Astronaut. 193 (2022) 691–703, http://dx.doi.org/10.1016/j.actaastro.2021.07.050.

[25] S. Wakitani, M. Deng, T. Yamamoto, Design of a data-driven controller for a spiral heat exchanger, IFAC-PapersOnLine 49 (7) (2016) 342–346, http://dx.doi.org/10.1016/j.ifacol.2016.07.320, 11th IFAC Symposium on Dynamics and Control of Process SystemsIncluding Biosystems DYCOPS-CAB 2016.

[26] S. Wakitani, T. Yamamoto, B. Gopaluni, Design and application of a database-driven PID controller with data-driven updating algorithm, Ind. Eng. Chem. Res. 58 (26) (2019) 11419–11429.
[27] M.-A. Cabrera-Rufino, J.-M. Ramos-Arreguín, J. Rodríguez-Reséndiz, E. Gorrostieta-Hurtado, M.-A. Aceves-Fernandez, Implementation of ANN-Based auto-adjustable for a pneumatic servo system embedded on FPGA, Micromachines 13 (6) (2022) http://dx.doi.org/10.3390/mi13060890.
[28] O. Rodríguez-Abreo, J. Rodríguez-Reséndiz, C. Fuentes-Silva, R. Hernández-Alvarado, M.D.C.P.T. Falcón, Self-tuning neural network PID with dynamic response control, IEEE Access 9 (2021) 65206–65215, http://dx.doi.org/10.1109/ACCESS.2021.3075452.
[29] J.A. Niembro-Ceceña, R.A. Gómez-Loenzo, J. Rodríguez-Reséndiz, O. Rodríguez-Abreo, A. Odry, Auto-regression model-based off-line PID controller tuning: An adaptive strategy for DC motor control, Micromachines 13 (8) (2022) http://dx.doi.org/10.3390/mi13081264.
[30] J.J. Castillo-Zamora, K.A. Camarillo-Gómez, G.I. Pérez-Soto, J. Rodríguez-Reséndiz, Comparison of PD, PID and sliding-mode position controllers for V–Tail quadcopter stability, IEEE Access 6 (2018) 38086–38096, http://dx.doi.org/10.1109/ACCESS.2018.2851223.
[31] J.R. García-Martínez, E.E. Cruz-Miguel, R.V. Carrillo-Serrano, F. Mendoza-Mondragón, M. Toledano-Ayala, J. Rodríguez-Reséndiz, A PID-type fuzzy logic controller-based approach for motion control applications, Sensors 20 (18) (2020) http://dx.doi.org/10.3390/s20185323.
[32] J.G. Ziegler, N.B. Nichols, et al., Optimum settings for automatic controllers, Trans. ASME 64 (11) (1942).
[33] H. Yu, Z. Guan, T. Chen, T. Yamamoto, Design of data-driven PID controllers with adaptive updating rules, Automatica 121 (2020) 109185, http://dx.doi.org/10.1016/j.automatica.2020.109185.
[34] D. Izci, B. Hekimoğlu, S. Ekinci, A new artificial ecosystem-based optimization integrated with Nelder-Mead method for PID controller design of buck converter, Alex. Eng. J. 61 (3) (2022) 2030–2044, http://dx.doi.org/10.1016/j.aej.2021.07.037.
[35] D. Izci, S. Ekinci, A.G. Hussien, Effective PID controller design using a novel hybrid algorithm for high order systems, PLoS One 18 (5) (2023) 1–21, http://dx.doi.org/10.1371/journal.pone.0286060.
[36] S. Ekinci, D. Izci, M. Yilmaz, Efficient speed control for DC motors using novel gazelle simplex optimizer, IEEE Access 11 (2023) 105830–105842, http://dx.doi.org/10.1109/ACCESS.2023.3319596.
[37] S. Ekinci, D. Izci, H. Baran, R.A. Zitar, A.R. Alsoud, L. Abualigah, Development of Lévy flight-based reptile search algorithm with local search ability for power systems engineering design problems, Neural Comput. Appl. 34 (2022) 20263–20283, http://dx.doi.org/10.1007/s00521-022-07575-w.
[38] I.H. Bell, J. Wronski, S. Quoilin, V. Lemort, Pure and pseudo-pure fluid thermophysical property evaluation and the open-source thermophysical property library CoolProp, Ind. Eng. Chem. Res. 53 (6) (2014) 2498–2508.